

University of New Mexico

UNM Digital Repository

Mechanical Engineering ETDs

Engineering ETDs

Fall 11-14-2022

Evolution of Shock-driven Multi-phase Instability

Joshua Chavez

University of New Mexico - Main Campus

Follow this and additional works at: https://digitalrepository.unm.edu/me_etds



Part of the [Mechanical Engineering Commons](#)

Recommended Citation

Chavez, Joshua. "Evolution of Shock-driven Multi-phase Instability." (2022).

https://digitalrepository.unm.edu/me_etds/219

This Thesis is brought to you for free and open access by the Engineering ETDs at UNM Digital Repository. It has been accepted for inclusion in Mechanical Engineering ETDs by an authorized administrator of UNM Digital Repository. For more information, please contact disc@unm.edu.

Joshua Chavez

Candidate

Mechanical Engineering

Department

This thesis is approved, and it is acceptable in quality and form for publication:

Approved by the Thesis Committee:

Peter Vorobieff, Chairperson

Mohan Gowtham

Darryn Fleming

Evolution of Shock-driven Multi-phase Instability

BY

Joshua Chavez

B.S., Mechanical Engineering, University of New Mexico, May 2021

Thesis

Submitted in Partial Fulfillment of the
Requirements for the Degree of

Master of Science

Mechanical Engineering

The University of New Mexico
Albuquerque, New Mexico

December 2022

Evolution of Shock-driven Multi-phase Instability

BY

Joshua Chavez

B.S., Mechanical Engineering, University of New Mexico, May 2021

M.S., Mechanical Engineering, University of New Mexico, December 2022

ABSTRACT

In many models and experiments using shock tubes and shock tube instabilities, measurements of velocity and position of the flow features are frequently taken in a single horizontal direction (or in one plane), however, the three-dimensional flow structure is important and cannot be fully resolved by such measurements. By placing a mirror at 45 degrees atop a test section of a shock tube, it becomes possible to visualize the flow from two directions simultaneously. The mirror is used to see if viable data can be gathered from the second view in conjunction with the main view. With high-speed video imaging, it becomes possible to visualize the three-dimensional structure of the shock interaction with the structure of interest, for example, a particle curtain. From the videos in conjunction with the pressure traces, the Mach number is verified, and the perturbation growth is measured from frame to frame. Through this method, shock driven instability can be observed. This provides the visual and experimental basis for validating numerical simulations including reduced-order instability models.

Table Of Contents

List of Figures.....	vi
List of Tables.....	viii
Chapter 1: Introduction.....	1
Section 1.1 Introduction To Shock and Instability.....	1
Section 1.2 Rayleigh-Taylor and Richtmyer Meshkov Instability.....	2
Section 1.3 Shock Driven Multiphase and Multiphase Rayleigh Taylor Instability,	3
Chapter 2: Experimental Setup.....	8
Section 2.1 Shock Tubes.....	8
Section 2.2 UNM Shock Tube 2022.....	8
Section 2.3 Experimental Viewing Methods.....	12
Chapter 3: Procedure.....	21
Section 3.1 Operation of Shock Tube and Camera.....	21
Section 3.2 Data Analysis.....	23
Section 3.3 Frame Rate Calculations and Time.....	27
Section 3.4 Mach Speed Verification.....	27

Chapter 4:Results.....	29
Section 4.1 Time duration and Frames	29
Section 4.2 Mach Speed Verification.....	30
Section 4.3 Ch2 Pressure Trace and Frames Plots.....	33
Chapter 5: Discussion.....	40
Section 5.1 Measuring Difficulties.....	40
Section 5.2 Differences and Non-linearity.....	40
Section 5.3 Agreement with Numerical Modeling.....	43
Chapter 6: Conclusion and Future Work.....	46
Section 6.1 Conclusion.....	46
Section 6.2 Future Work.....	47
References.....	49

List of Figures

Figure 1: Classic Example of Rayleigh-Taylor Instability.....	4
Figure 2: Classic example of Richtmyer-Meshkov Instability.....	5
Figure 3: Example of Multiphase-Rayleigh-Taylor Instability.....	7
Figure 4: Diagram of the UNM Shock Tube 2022.....	9
Figure 5: Rigoll DS1204b oscilloscope.....	11
Figure 6: Test section before modification.....	12
Figure 7: Problematic First Viewing Method.....	14
Figure 8: Distorted Top View.....	15
Figure 9: 45-Degree Angle and Mirror.....	16
Figure 10: Clear 45-Degree Photograph.....	17
Figure 11: No Bracket Blocking Camera.....	18
Figure 12: Clear Earlier Frame Instability.....	19
Figure 13: Escaping Shock Wave.....	20
Figure 14: 2mm Curtain Particle Feeder.....	21
Figure 15: Driver Section Camlock.....	22
Figure 16: Side Test Section View.....	25
Figure 17: Top Test Section View.....	25

Figure 18: Side View Plot Mach 1.2 2mm Curtain.....	34
Figure 19: Top View Plot Mach 1.2 2mm Curtain.....	34
Figure 20: Side View Plot Mach 1.45 2mm Curtain.....	35
Figure 21: Top View Plot Mach 1.45 2mm Curtain	35
Figure 22: Side View Plot Mach 1.7 2mm Curtain	36
Figure 23: Top View Plot Mach 1.7 2mm Curtain.....	36
Figure 24: Side View Plot Mach 1.2 6mm Curtain.....	37
Figure 25: Top View Plot Mach 1.2 6mm Curtain.....	37
Figure 26: Side View Plot Mach 1.45 6mm Curtain.....	38
Figure 27: Top View Plot Mach 1.45 6mm Curtain	38
Figure 28: Side View Plot Mach 1.7 6mm Curtain.....	39
Figure 29: Top View Plot Mach 1.7 6mm Curtain.....	39
Figure 30: Frame Progression Combined view.....	41
Figure 31: Pressure Projection.....	43
Figure 32: Pressure Trace Mach 1.45.....	43
Figure 33: Cloud Expansion Length after Time.....	44
Figure 34: Theoretical Expanded Cloud.....	45

List of Tables

Table 1: Numbered Pressure Transducer and Distance From Particle Curtain.....	10
Table 2: Number of Frames and Total Time Duration	29
Table 3: Time Delay of Pressure at The Curtain.....	30
Table 4: Mach 1.2 2mm Mach Speed Validation	31
Table 5: Mach 1.45 2mm Mach Speed Validation.....	31
Table 6: Mach 1.7 2mm Mach speed Validation.....	32
Table 7: Mach 1.2 6mm Mach speed Validation.....	32
Table 8: Mach 1.45 6mm Mach speed Validation	32
Table 9: Mach 1.7 6mm Mach speed Validation.....	32

Chapter 1: Introduction

Section 1.1 Introduction to Shock-Driven Instabilities

There are many reasons to study shock-driven hydrodynamics, but one application that stands out due to its recent importance is the scramjet (Nair, Narayanan, and Suryan 2021a). Combustion at supersonic speeds can be somewhat of an issue. With the scramjet, shock reflections, shear, and expansion waves can be used to facilitate and control combustion at hypersonic speeds. One configuration requires inserting a jet injector for combustible gas so that it improves the mixing effectiveness inside the combustion chamber without pressure loss. This is especially important when accelerating and decelerating, as external pressure waves could cause shock instability, which could either help mix the injected gas or disperse the gas so much that it is incombustible. In addition, it is important to understand how the instabilities might interact with the mixing in hypersonic engines. This is like clapping in front of a candle to put it out. The pressure wave is what extinguishes the flame. This can happen in one of these engines, why is important to understand the instability it would exhibit in flight and prevent flameout (Mbagwu, Chukwuka, and James F. Driscoll 2016). It is also important to consider that in scramjets, a multiphase gas mixture must be studied, as the fuel could be a gas, liquid, or even solid, although most of the time it is most likely an interaction between a liquid fuel and air (Nair, Narayanan, and Suryan 2021a).

A second form of application is shock mitigation in explosive munitions storage. In one study, it was found that explosives under water could bring a reduction in static

over pressure of 70 percent. The water gas interface would be considered a multiphase region with the explosion causing a shock wave, which by default, would cause the shock driven instabilities in the area. This means that at the interface referenced, the density ratio on the interface, depending on volume, fluid, liquid or gas, could potentially produce the flow regime necessary for the instabilities to form. This idea has far-reaching effects as it means that the type of explosive storage would change as well as the size of the cache itself would increase (Xu et al. 2021).

The classical instabilities, Rayleigh-Taylor (RTI) and Richtmyer-Meshkov (RMI), occur on a density interface between two gases or fluids accelerated by gravity (RTI) or shock (RMI). In this classical formulation, the key characteristic of the interface is the Atwood number. The Atwood number, by definition, is the dimensionless ratio of the difference in mass densities of heavy (ρ_2) and light (ρ_1) gas at a boundary.

$$A = (\rho_2 - \rho_1)/(\rho_2 + \rho_1) \quad (1)$$

The condition necessary for RTI and RMI to emerge is that the densities cannot be equal. In these flow regimes, the Atwood number varies between zero and one.

A generalization of RTI and RMI to multiphase flow is possible. In this case, the interface separates areas where **average** density varies due to particle or droplet seeding. In the limit case of small particle size, the flow behavior is similar to that of classical RMI and RTI, manifesting similar nonlinear growth rate (Anderson et al. 2015; Vorobieff, Rightley, and Benjamin 1999). However, earlier results were acquired at modest mass loading due to particles, with the volume of interest primarily containing

gas. While running experiments, it is unclear what would happen if the conditions were different.

By analogy with the classical case (Eq. 1), consider a multiphase Atwood number

$$A_m = (\rho_s - \rho_u)/(\rho_s + \rho_u)$$

Here the subscripts s and u refer to seeded versus unseeded gas. For example, if the multiphase Atwood number was approaching 1, the mass loading would be dominated by particles instead of gas, as seen before. With this change, would classical fluid dynamics still hold (Vorobieff et al. 2020; Freelong 2021)? The particle inertial effects would be much greater. This implies that the particle dynamics could dominate the relevant physics, superseding the dominance of hydrodynamic effects at $A_m \sim 1$.

Section 1.2 Rayleigh-Taylor and Richtmyer Meshkov Instability

In fluid mechanics, RTI and RMI are classical examples of interfacial instabilities. These instabilities are the simplest cases: they occur in a single-phase medium containing differing densities of liquids and can be explained by two-dimensional ideal flow theory. In some special cases, a very light and heavy liquid can be used to demonstrate a model- like air and water which can place it in the realm of what is known as multiphase (I.G. Currie 2013).

RTI was first measured and analyzed by Lord Rayleigh in the late 19th century and explained theoretically by G.I. Taylor in 1950. RTI is characterized by three stages.

The first is linear perturbation growth (Zhou et al. 2021), followed by a stage of non-linear growth, where RTI manifests a distinctive flow structure, creating spike- like striations or streaks within the fluid interface due to gravity or impulse (Ludwigsen et al. 2022).

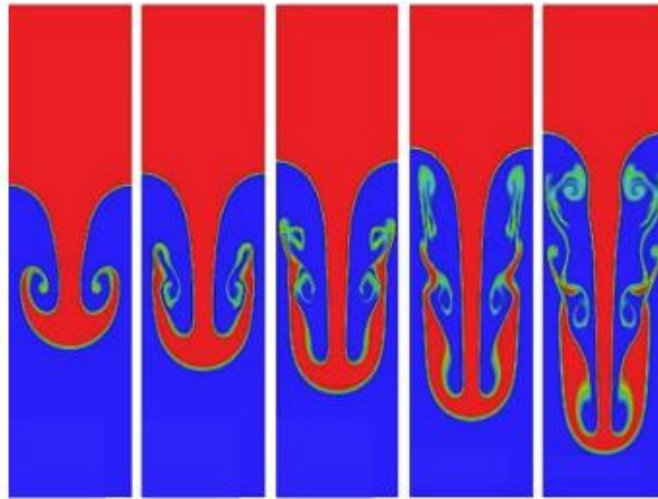


Figure 1: Classic Example of Rayleigh-Taylor Instability(Zhou et al. 2021)

The Richtmyer-Meshkov Instability (RMI) is a special case of Rayleigh Taylor instability. RMI was first found and analyzed at Los Alamos National Laboratories in the 1960's by Dr. Robert D. Richtmyer and in Sarov Nuclear Center (Russia) by Dr. Evgeny E. Meshkov (Meshkov 1969). This is a case of impulsively accelerated Rayleigh-Taylor Instability, leaving it to maintain the features described, except it has somewhat of a different appearance and growth rate (Orlicz, Balasubramanian, and Prestridge 2013). It is often accompanied by the RTI, yet it is characterized by its distinctive mushroom shape, see Figure 2 (Vorobieff et al. 2010). Typically, as the shock impulse crosses the fluid boundary, the denser liquid forms small spikes in the less dense one. As the spike grows it forms a type of bubble which due to reflected shocks within the interfaces and the two mediums, the bubble begins to grow while simultaneously leaving swirling and

mixing vortices toward the bubble's edges where the spikes are lagging. This bubble and vortex formation is what makes RMI have its shape (Brouillette 2001).

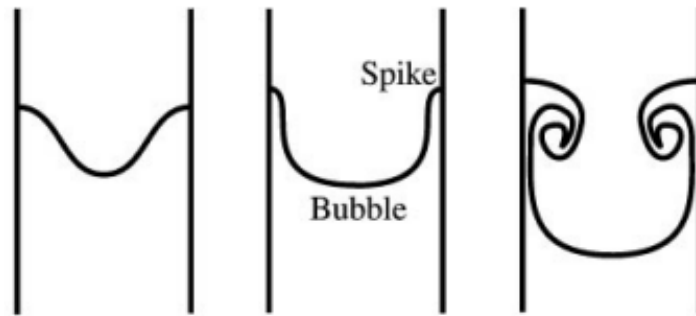


Figure 2: Classic example of Richtmyer-Meshkov Instability(Brouillette 2001)

Section 1.3 Shock Driven Multiphase and Multi Phase Rayleigh Taylor Instability

These shock driven instabilities are present in many real-world applications where turbulent mixing is present or necessary. For example, they can be found in plasma mixing in stars and supernovas, in fuel-oxygen mixing in supersonic combustion engines, inertial fusion, and pulsed power (Musci et al. 2020).

As mentioned earlier, there are many different applications for multiphase shock instability research. Much of the research seems to be centered on gas mixing and diffusion in an area. This is especially crucial when moving at speeds faster than the speed of sound. In addition, both for rocket propulsion and for blast mitigation it is important to understand shock-driven instability. It is important to understand how engines, vessels and housings behave during these high-speed interactions, as premature detonation is not the intended purpose (McFarland et al. 2016; Zhou et al. 2021).

Shock Driven Multiphase Instability is a relatively new field of study. It occurs in many natural environments and is important for many applications, such as hypersonic engines and shock mitigation, as mentioned earlier. It involves sending a shockwave through a mixture of gases, fluids, droplets, and particles (I.G. Currie 2013). In most cases, it is like RM and RT in that it is a result of constant or impulsive acceleration normal to a boundary. The important difference is that, while in the case of RMI and RTI, the boundary is between two gases or liquids of different density, in the multiphase case it is the average density of the medium that changes across the boundary (for example, between pure air and air with particles or droplets). In the experiments described in the next chapters, the instability is due to shock traveling through unseeded air and traversing a falling particle curtain at varying Mach speeds including Mach 1.2, 1.45, and 1.7 (Freelong 2021). In previously published papers, it was found that, in exploring the Multiphase-Rayleigh Taylor instability (the multiphase analogue to the standard Rayleigh Taylor instability that leaves characteristic finger-like striations), a flow regime with a previously unobserved instability growth rate may exist (Vorobieff et al. 2020).

The paper written in 2020 was a joint effort by the University of New Mexico and San Diego State University. The idea was to measure the perturbation growth of falling

particles as well as the sustained acceleration growth of the instability due to gravity. For a visualization see Figure 3.



Figure 3: Example of Multiphase-Rayleigh-Taylor Instability(Vorobieff et al. 2020)

This instability growth was then tracked based on a frame measurement method in the image processing software, FIJI. By tracking the leading and the trailing edge of the curtain as the curtain fell from frame to frame, it was possible to see a trend in the particle growth rate. This trend, when graphed, seemed to be linear, with the r^2 value for the linear fit between .95 and .98. For that flow regime the multiphase Atwood number was close to unity. A simple theoretical explanation for the trend was provided, based on the assumption that the growth of perturbation is dominated by gravity-accelerated particle movement. Because of the similarly high value of A_m in the experiments described below, a similar method of analysis will be used as the basis for the shock-driven experiments here (Vorobieff et al. 2020).

Chapter 2: Experimental Set Up

Section 2.1 Shock Tubes

Shock tubes are typically used to create and monitor shockwaves traveling faster than the speed of sound (767 mph for air under standard conditions) through a medium. Usually, the shock tube utilizes a driver section, which is used to build up a desired amount of pressure. In many shock tubes, the driver section also uses a diaphragm of varying thicknesses and a puncture mechanism within the section to instantaneously release the pressure to cause the shock wave (I.G. Currie 2013). Many of the experiments allow to capture high speed video or single images using lasers and high-speed cameras. By taking each individual frame from the video, images can be extracted and used to calculate velocity, position, density, acceleration, types of instability, streamline, and many other characteristics of the flow. These can be used to validate analytical and numerical models and allow for more precise and accurate simulations to be produced.

Section 2.2 UNM Shock Tube 2022

The shock tube at the University of New Mexico (August 2022) has many similarities to other shock tube setups that have been used in the past by UNM. It has a square 76.2×76.2 mm cross-sectional area, uses nitrogen as a driver gas for the experiments described here, a Chronos high-speed camera, a particle shaker, a particle collection box, a round driver section (to better withstand pressure), a diaphragm, and a puncturing mechanism, which is a pneumatic piston driven arrowhead aimed at the center of the diaphragm. The diaphragm in these experiments was chosen based off a trial-and-error method, pressurizing different thicknesses of diaphragms until they burst on their own. The diaphragm for 1.2 burst around 50 psi, the 1.45 around 120 psi, and the 1.7

around 200 psi. For Mach 1.2 the corresponding diaphragm thickness is .0508mm, for Mach 1.45 the diaphragm thickness is .127mm and lastly for Mach 1.7 it corresponds to .254mm . The main difference between this rig and past ones is that, most recently in January of 2022, the tube extends into a baffle box (Freelong 2021) designed to suppress reflected shock.

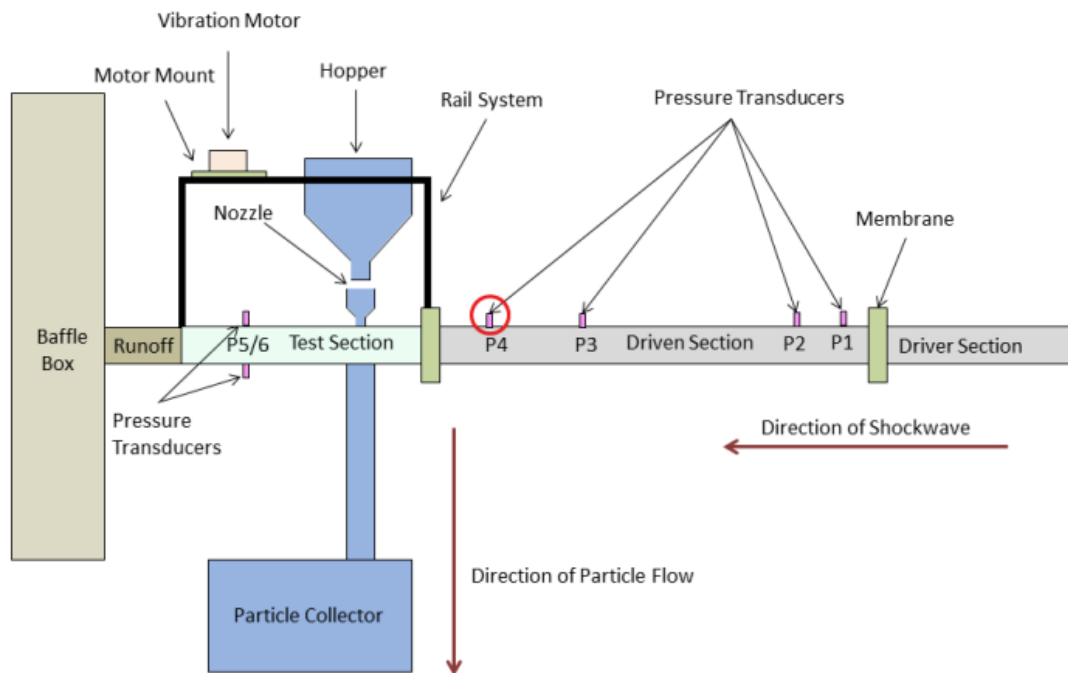


Figure 4: Diagram of the UNM Shock Tube 2022(Freelong 2021; Ludwigsen et al. 2022)

This rig has the added benefit of being very modular and many different experiments can be run with easily switchable setups. The goal of the work described below was to improve visualization by allowing simultaneous imaging of the flow from multiple directions. The second view realization has gone through three iterations due to several issues including vibration, ease of setup, and available space. Currently the mirror is placed on top of the test section with a 135-degree angle bracket to achieve the 45-degree view with the camera. The camera was also changed, from a single-exposure

Apogee camera in older experiments. It is now a faster, more sensitive high speed video camera (Chronos 2.1 which can take 1000 fps at 1920x1080 resolution; however, these values can be modified for faster framerates and reduced resolution combinations)(“USER MANUAL CHRONOS 1.4 & CHRONOS 2.1-HD,” n.d. 2021)

For the Shock-Driven Multiphase Instability experiments at UNM, the system is in the configuration with nitrogen as its driver gas. The main tubing housing is comprised of Al-6061-T6 alloy (Freelong 2021). This tube is powder coated with a black coating, enabling better visualization. As described above, an arrowhead attached to a pneumatic piston punctures the diaphragm and releases the pressure behind the diaphragm. This allows the shock wave to flow toward, hitting either a particle curtain, an array of solid bodies (Rahman et al. 2021), or a glass pane (Shaheen 2023), which are the other experiments currently in progress. The test section is where the visualization takes place. It has a clear top and side portion. These two panels are made from acrylic. In earlier experiments, polycarbonate was also used. The shock wave is discharged into the baffle box filled with porous material to absorb the reflected shock.

Pressure Transducer	P3	P4	P5/6
Distance (m)	1.307	.596	.583

Table 1: Numbered Pressure Transducer and Distance From Particle Curtain

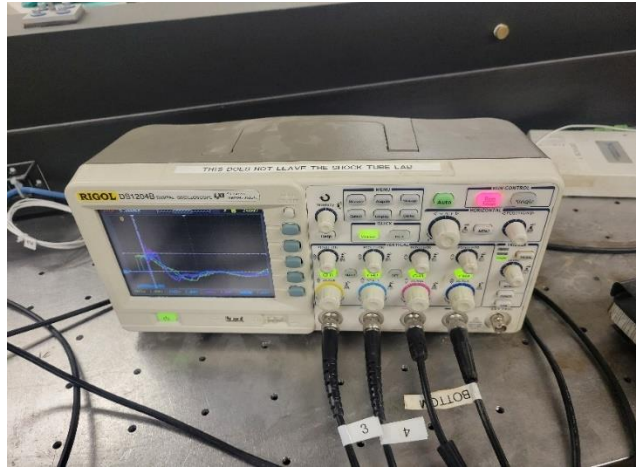


Figure 5: Rigol DS1204b oscilloscope

In some configurations, the shock tube can be capped instead, and a re-shock can be measured using pressure traces taken from pressure transducers (see Table 1). For the experiment in our case, four pressure transducers are used. They are the 3, 4, 5, and 6 in the image above, using a Rigol DS1204b oscilloscope commonly found in a laboratory setting to record the pressure traces (see Figure 5) (“RIGOL User’s Guide DS1000B Series Digital Oscilloscopes” 2016). The channel designation for these trials is channel 1, channel 2, channel 3, and channel 4 (see Table 1 above). These correspond to pressure transducer 3, 4, 5 and 6, respectively, as shown in the setup above. In Figure 6, the setup is ready to be outfitted with the top viewing configuration which will be shown later. This can be seen because the top of the test section in the image is clear, as well as the side view.

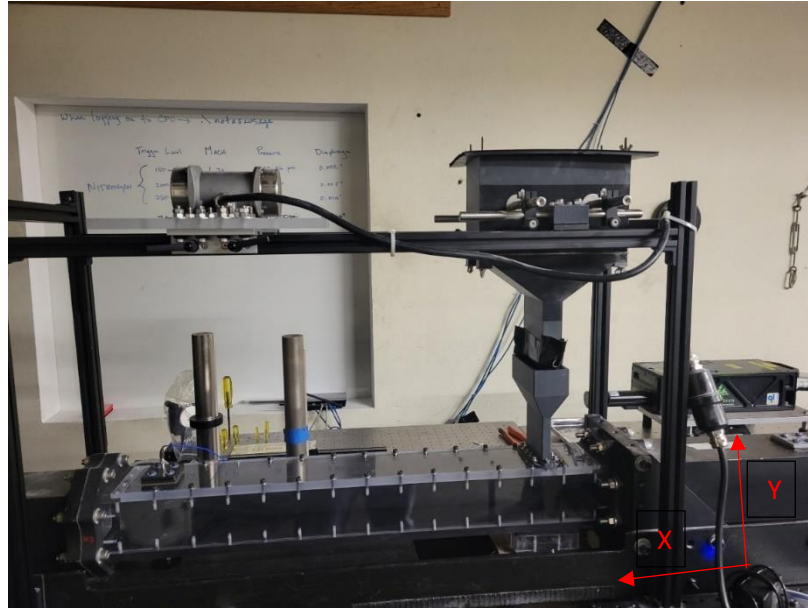


Figure 6: Test Section Before Modification

Section 2.3 Experimental Viewing Methods

Experimental Method 1:

Prior to designing the first experimental stand for the 45-degree angle mirror for the top view of the test section, some deliberation took place between several of the team members. Something which seemed to be agreed upon was to keep it simple as well as keep it relatively cost efficient. In doing so, the first iteration was then decided upon and built with the understanding that this would allow the reflection of the top of the test section and the side view to be seen simultaneously. Some of the pictures below contain images from the solid body shock experiments of Mohammad Rahman as this portion was fielded before the experiments of the particle curtain (Rahman et al. 2021).

As mentioned, three methods have been introduced to visualize the top view of the test section. The first method involves the current shock tube configuration with

almost no change whatsoever. The change is the addition of a mirror that would be tilted at a 45-degree angle in the direction of the camera. By adjusting the focus, focal depth, and visual area of the camera, it is then possible to view both the side plane as well as the top plane. This is beneficial in shock experiments because characterizing the shock propagation through the tube can now be monitored using the X, Y and X, Z planes.

The set up for this model involved a camera tripod as well as several adjustable pipes and pipe clamps attached to each other to attain the proper angle. The tripod was approximately 2 feet tall with an adjustable height up to 6 feet tall. If the mirror needed to be placed on the ground, it could be set to any height in between those ranges. The pipe clamps were each roughly 8-12 inches in length, and when the clamps were tightened sufficiently, it would keep the 45-degree angle. One of the pipes had a small clamp that grasped the plate which was epoxied to the back of the mirror. This enabled the user to maintain hold on the mirror while also maintaining the height (see Figure 7).



Figure 7: Problematic First Viewing Method

Findings on the first model indicated that this, unfortunately, was not a viable experimental setup as, upon use, there seemed to be several issues that could not be remedied for a variety of reasons. The first reason being that the setup was not conducive to a clear mirror. Where the prior experiment had been used to drop particles into the view of the camera, this one did not require that. Because of this, residual particles and debris not cleaned off properly stuck to the reflective side of the mirror. This meant that, after every run, the mirror needed to be cleaned off. Additionally, the angle would have to be readjusted every time, as well as the stand angle. The second issue was that, after each shock, the test section would vibrate everything around it to a certain degree. This did two things. It meant that the mirror must be reset each time as well. Ultimately, this

indicated that after each run of the shock tube, the mirror must be reset at least once. The second issue is that when high speed video is being taken, it meant that the shock tube vibrated the stand which the mirror was attached to, prior to the shock reaching the test section. By default, the mirror was also vibrating at the same time as the frames being taken and the picture is not particularly clear. This is what is believed to cause the distortion in Figure 8 below.

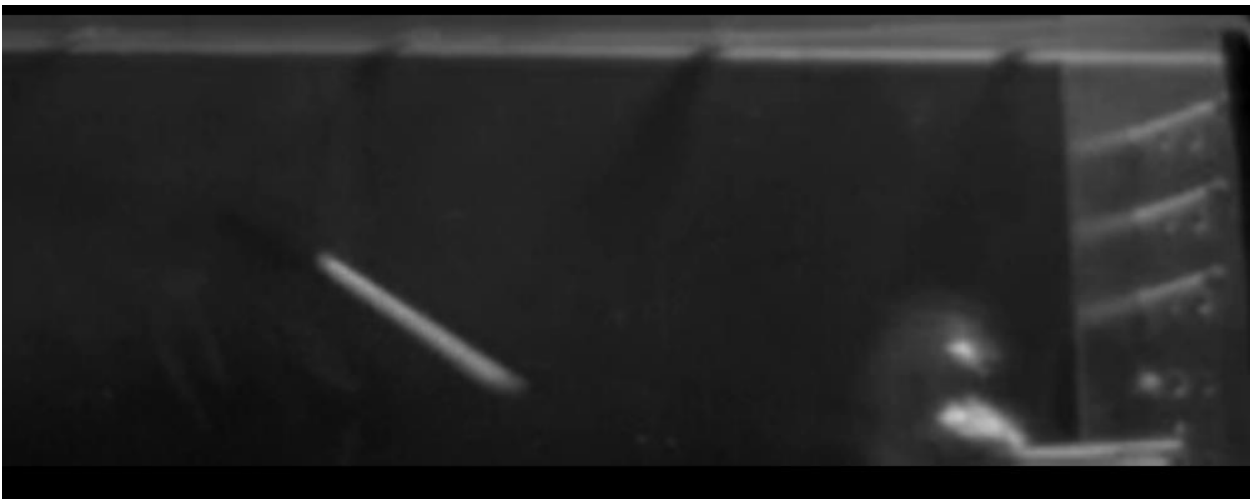


Figure 8: Distorted Top View(Rahman et al. 2021)

Ultimately, because of these issues, the first iteration of the 45-degree angled mirror to view the top of the test section was deemed to be too problematic, and thus impractical to use.

Experimental method 2:

With the second method of experimental view, the simpler option seems to be of a more beneficial nature. The general requirement for the second view is only that it is possible to see two views in the same frame simultaneously. Seeing as the previous issues now became known, making sure that the new stand will not move, vibrate, or become

dirty became the new objective. It was decided that a simple fixture be added to the test section directly. The top portion of the test section is removable, so this whole piece will be modular and other test sections can be replaced.



Figure 9: 45-Degree Angle and Mirror(Rahman et al. 2021)

The setup involves placing a 45-degree angle stock and double-sided tape. Sticking the angled piece to the test section out of view of the reflection needed ensured a clear image. Using another piece of tape and placing the mirror on it should ensure that the mirror is stable and will not have to be reset routinely. The new test section will ensure that the mirror does not get dirty either as the test section does not have a close opening to the mirror. The double-sided tape, if it is thick, will function as a damper. This will ensure that the mirror does not vibrate when the frame is being taken. From a test run that was taken, it was verified that this is a viable option for viewing the top plane of the

test section, and none of the problems previously encountered became an issue as shown (see Figure 10). It is a lot clearer and does not contain the same distortion.

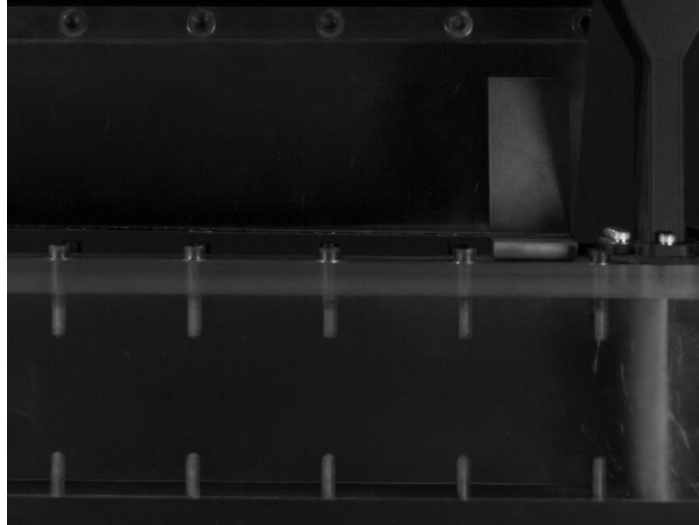


Figure 10: Clear 45-Degree Photograph

Third method:

As seen in the previous method, the view is very clear and stable. However, this seems to have one major drawback. This is the fact that the instability early in the video is hidden in the reflection as the bracket would block it entirely. The most interesting growth occurs in the early frames of the video which means significant portions of the instability is missed entirely. As shown below the bracket is no longer covering in (Figure 11).



Figure 11: No Bracket Blocking Camera

This method modifies the previous bracketing system. Instead of the 45-degree angle bracket, a bracket of 135 degrees is placed on the back of the test section. The mirror is placed on the inner portion of the 135-degree angle bracket. This means that the mirror will be at a 45-degree angle. This method does not interfere with imaging the early instability growth. This setup maintains all the stability and clarity of the second method, with the added benefit of being clear of the bracket itself in the camera frame - it is now possible to see the earlier frames as seen in Figure 12.

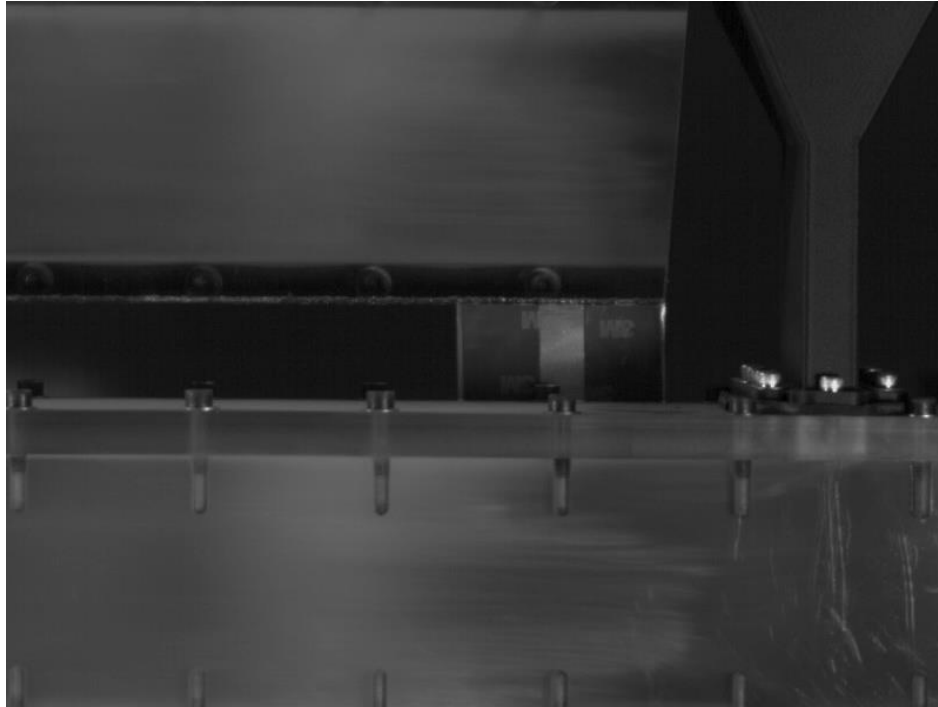


Figure 12: Clear Earlier Frame Instability

Initially, with this method, it seemed very promising, however there was one major flaw that had to be dealt with, which the second method did not have. The brackets for the second method were directly attached to the top panel, and the entire mirror and bracket combination moves as the panel does. This is important because when screws are removed from the test viewing section to place the mirror, it was found that this movement was of a significant consequence with only the third view. The shock wave escapes out of the side of the panel least fastened. The second view moved with the panel, and the third view did not. This left a mangled and broken mirror in its wake. The moving panel can be seen in Figure 13. This difference can be seen in the image to the right. The shock lifts the entire panel on the back side. Both mounts were fastened to the section with double sided 3M tape. The 3M tape also seemed to act like a damper. The

mirror vibration was minimized because of this. For vibration purposes it was like attaching a damper to a cantilever, leaving a relatively steady image. The mirror was also moved slightly up above the screws so more could be used to fasten the panels. It also has the added benefit of increasing the distance from the shockwave. As shown below in the video, the snapshot becomes very clear. These shock driven striation growths can also be seen very clearly in this frame as well as the cloud which will be mentioned in later chapters.

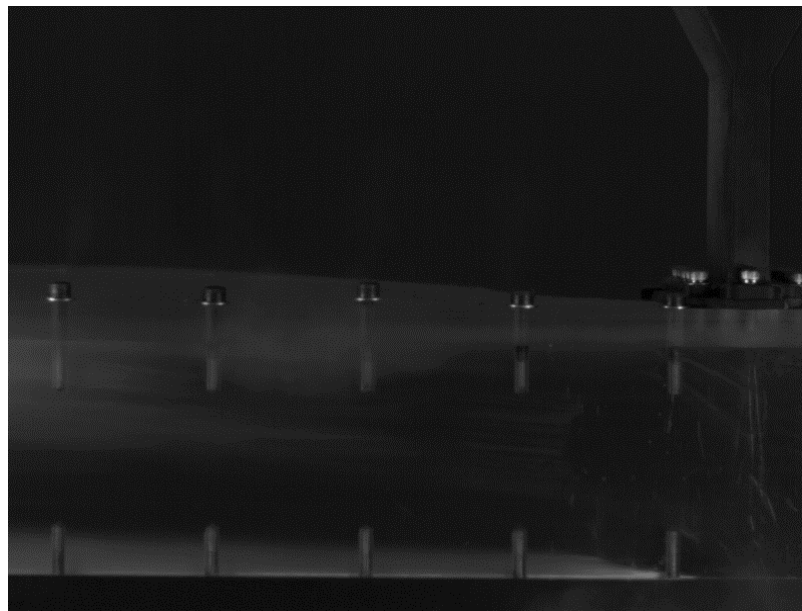


Figure 13: Escaping Shock Wave

Chapter 3: Procedure

Section 3.1 Operation of Shock Tube and Camera

To begin, it is necessary to use the proper thickness of diaphragm for each Mach number. The diaphragm for 1.2 corresponds to the thickness of .0508 mm at .172369 MPA. The 1.45 diaphragm corresponds to the .127 mm thickness at .5515 MPA. Lastly, the 1.7 Mach number corresponds to the .254 mm diaphragm at 1.31 MPA. The driver gas can be nitrogen or helium. For our experiments, nitrogen was used. In many of these experiments, each method of viewing the top is used in a progression which resulted in the final viewing method. This means the result of the top view will be mixed between the three types of viewing methods.

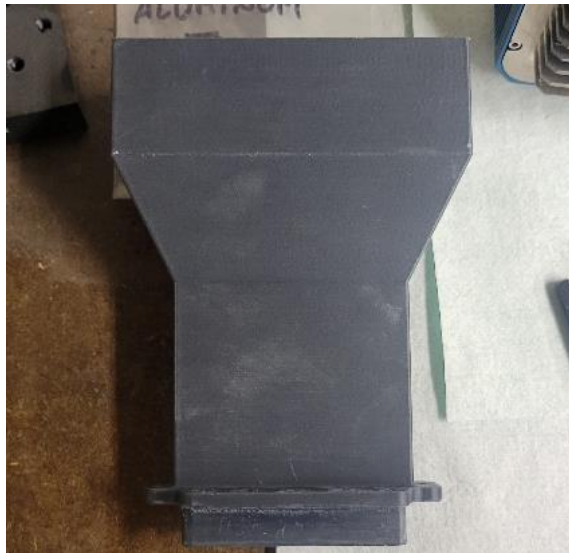


Figure 14: 2mm Curtain Particle Feeder

To begin the experiment, a particle curtain funnel width is chosen between 2 mm and 6 mm, as shown in Figure 14. In the first case, it is 2 mm and the second case was 6 mm, with both using 30–50-micron particles (Freelong 2021) .The funnel is then bolted

to the top of the test section out of the way of the mirror. The camera frame is set to contain both the top and side planar views. It had a framing rate of 4352 fps and resolution of 800 x 600. In addition, it is necessary to check if the images are clear enough to see the curtain. Based on the desired Mach number, pressure and diaphragm thickness are set to the necessary values.

The diaphragm is placed between the driver section and the shock tube. The driver section is locked into place using the securing mechanism on the flanges, which consists of two camlocks, one on each side as shown below (see Figure 15). The oscilloscope-connected pressure transducers are checked to see if they are working properly. The driver section can now be pressurized to the desired pressure. The shaker box is then turned on. It is necessary to wait for the curtain to achieve steady state before pressing the recording button on the camera. Finally, one presses the trigger and after shock interaction turns off the recording. The user then saves the video to a computer file and checks for clarity and verifies that the pressure traces are consistent with the Mach numbers.

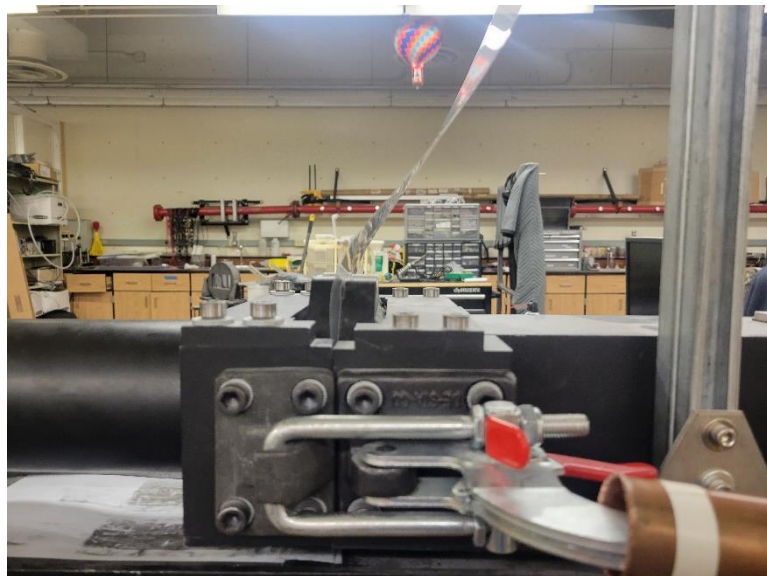


Figure 15: Driver Section Camlock

Section 3.2 Data analysis

In measuring the shock driven instability in the videos, it was necessary to split the videos up to determine the starting frame and ending frame. In doing this, each video was watched to find around the whereabouts of the frames based off the time stamp in the video. Following finding the starting time stamp, a directory was made to which the video frames would be kept. A code in the ffmpeg command package was used to extract the frames(FFmpeg Developers 2016). The video time stamp is not real time because the videos are encoded by the camera to play at 60 frames per second regardless of the actual framing rate. After that, the frames have to be visually found in the directory and catalogued. The frames of no use are then deleted. The background image from the frames is then picked, one which has no particles in the frame.

Next, by using the FIJI program set of ImageJ, all the frames were then placed in stacks. The chosen background images of each stack were then subtracted from the entire set of stacks. This ensures that there is no mix up of what particles are moving and what may be stationary particles left over from earlier experiments: the shock tube is cleaned before every run, but sometimes it is difficult to remove all the particles. Once the background is subtracted, each stack is then separated into the top view and side view of the experiment. They are then duplicated to isolate and zoom into the image. This leaves two separate stacks which contain the top and side views respectively. The stacking process makes it easy to take measurements in one frame and move to the next frame and do the same. In ImageJ, the contrast and visual effects were set to automatic so that

viewing was clear. Much of this involves learning the Image J processing software with the FIJI Package (Schindelin et al. 2012).

The measurement process entailed finding the first frame of when the shock driven instability can be measured. This was the frame where it is possible to visually see the small striations and spikes previously referenced. The leading edge and trailing edge of the instability were then measured using the bounding box mechanism in FIJI, much like in the Fractal properties paper. Using the width coordinate of the box, the measurement was then written down (Ludwigsen et al. 2022). The measurement was taken for as many different striations as possible. The average was five per frame. Once the measurements were taken, the standard deviation and average were then calculated.

The frames displayed below are the actual frames used to measure the instability growth leading edge to trailing edge. Note that here the instability is measured at the trailing end of the curtain, as its upstream end contains diffuse and highly reflective small particles making similar measurement difficult. Thus the leading edge and trailing edge refer to the bounding box for the perturbed trailing end of the curtain. Using the Fiji measurement tool it is very easy to measure the tip to tail of the instability. This process is used for both side and top views of the videos. In each frame at least five to six measurements were taken and averaged to produce each data point in the graphs. The method is demonstrated below with one of the Mach 1.2 6 mm curtains with the side and top views respectively (see Figure 16 and 17). The first 3-5 frames of most of the top views is un-usable as the mirror does not pick up the curtain until a few more frames after the initial shock impact to the curtain. Both views are side by side for some comparison.

As the shock passes the instability grows. Each measurement from ImageJ is in units of pixels. This can be seen in both views although the side view is much clearer.



Figure 16: Side Test Section View



Figure 17: Top Test Section View

After the measurements were made, they were then plotted with error bars denoting the standard deviation between the average of the instability amplitude in each frame. This helped to see the difference in variation from frame to frame, similar to earlier studies (Ludwigsen et al. 2022; Freelong 2021). This was done for both the side and top views.

In graphing the averages and standard deviation, the pressure trace was also plotted on the same graph as the instability growth. This was done to show where the shock begins to interact with the curtain. To adjust for the shock interaction time, a time shift was necessary, as it will be described in the next section. The channel 2 pressure transducer 4 pressure trace is .596 m from the shock curtain. This means that, to set the graph to the correct time, adding the shock travel time from the transducer to the curtain is necessary. This is found by dividing the distance by the velocity of the ideal shock wave used. In this case, it is Mach 1.2 or 411.6 m/s, 1.45 or 497.35 m/s and 1.7 or 583.1 m/s, which is used to calculate the time to cover .596 m. By visual inspection, the first frame of the shock interaction is taken to be the ideal point of interaction, and the graphs are then matched up at that point. As it is shown in the results portion, the pressure trace corresponding to the shock is somewhat earlier than the instability becomes visible.

Section 3.3: Frame Rate Calculations and Time

The camera frames were calculated to be .0002 seconds roughly by dividing the total number of frames where something could be measured by the frame rate of 4352 fps. To find the interval between points divide that again by the number of frames used. The different sets over all the time were consistent.

$$Time\ Observed = \frac{numberofframes}{frames\ per\ second} (2)$$

$$Interval = \frac{TimeObserved}{numberofframes} (3)$$

This becomes somewhat important when deciding where and how to graph the pressure trace. The initial spike correlates to the initial frame.

The projected time instance of impact of the pressure wave is off because the sensor is .596m from the actual curtain so the time of impact is going to be delayed. This delay is calculated by taking the distance .596m and dividing by the nominal shock speed in meters per second. The ideal Mach speed for Mach 1.2 is 411.6 m/s.

$$Timedelay = \frac{.596m}{MachSpeed(\frac{m}{s})} (4)$$

Section 3.4: Mach Speed Verification

The process for verifying the Mach Number is as follows. The time between the first and second pressure signal is found using the pressure data and comparing when the

pressure spikes to a positive voltage. Each cell in the excel spread sheets corresponds to a .0001 second increment. Now using time counting how many cells to the first spike of the next signal divide this by a known quantity of distance .7112m between the sensors the Mach number can be verified.

$$MachSpeed \left(\frac{m}{s} \right) = \frac{Timeelapsed}{.7112m} \quad (5)$$

Delay		
1.2	1.45	1.7
0.001451	0.0012	0.001023

Table 3: Time Delay of Pressure at The Curtain

A time adjustment is necessary because the closest pressure transducer is .596m between the curtain and the second sensor. The adjustment would be seen as a time delay in the signal graph as the distance has yet to be traveled (see Table 3 and Equation 4). This is where the shock wave is projected to hit the curtain, given the stated Mach number and distance.

Section 4.2 Mach Speed Verification

Mach speed is calculated by finding the number of time data points between the first two sensors. In this case, they will correspond directly to millisecond time intervals. Through using the time data and the distance traveled between transducers, the proceeding case is .7112 m. This same process is used for all Mach speed and curtain size combinations. For the equation (see Equation 5) in the previous chapter, there are six data sets in total. It is important to note that the number of trials only reflects the number of usable pressure traces. Some of the files became corrupted and were rendered un-usable which is why some trials are missing in the tables.

The first table in the sequence shows the calculated Mach speed for the 2mm curtain at the ideal Mach speed of 1.2.

2mm Mach 1.2									
Trial	1	2	3	4	5	6	7	9	
Speed	1.21	1.22	1.21	1.21	1.21	1.29	1.29	1.21	
Speed(m/s)	415.0	415.0	415.0	415.0	415.0	442.5	442.5	415.0	

Table 4: Mach 1.2 2mm Mach speed Validation

The second table in the sequence shows the calculated Mach speed for the 2mm curtain at the ideal Mach speed of 1.45.

2mm Mach 1.45									
Trial	1	3	4	5	6	7	8	9	13
Speed	1.38	1.39	1.38	1.48	1.39	1.38	1.39	1.39	1.39
Speed(m/s)	473.3	476.8	473.3	507.6	476.8	473.3	476.8	476.8	476.8

Table 5: Mach 1.45 2mm Mach speed Validation

The third table in the sequence shows the calculated Mach speed for the 2mm curtain at the ideal Mach speed of 1.7.

2mm Mach 1.7									
Trial	1	2	3	4	5	6	7	8	9
Speed	1.59	1.59	1.59	1.59	1.59	1.59	1.59	1.59	1.59
Speed(m/s)	545.4	545.4	545.4	545.4	545.4	545.4	545.4	545.4	545.4

Table 6: Mach 1.7 2mm Mach speed Validation

The fourth table in the sequence shows the calculated Mach speed for the 6mm curtain at the ideal Mach speed of 1.2.

6mm Mach 1.2					
Trial	5	6	7	8	9
Speed	1.21	1.21	1.29	1.21	1.29
Speed(m/s)	415.03	415.03	442.47	415.03	442.47

Table 7: Mach 1.2 6mm Mach speed Validation

The fifth table in the sequence shows the calculated Mach speed for the 6mm curtain at the ideal Mach speed of 1.45.

6mm Mach 1.45								
Trial	2	4	5	6	7	8	9	10
Speed	1.38	1.39	1.39	1.38	1.38	1.48	1.38	1.38
Speed(m/s)	473.34	476.77	476.77	473.34	473.34	507.64	473.34	473.34

Table 8: Mach 1.45 6mm Mach speed Validation

The sixth table in the sequence shows the calculated Mach speed for the 6mm curtain at the ideal Mach speed of 1.7.

6mm Mach 1.7						
Trial	1	2	3	4	6	7
Speed	1.76	1.59	1.73	1.59	1.59	1.59
Speed(m/s)	603.68	545.37	593.39	545.37	545.37	545.37

Table 9: Mach 1.7 6mm Mach speed Validation

Section 4.3 Ch2 Pressure Trace and Frames Plots

Some of the videos were un-usable as no leading or trailing edges were able to be seen. Only the videos where data could be gathered are used in the graphs. Only one example of each will be shown here, because, after seeing one graph, the trend seems to stay decently consistent without much change. The exception is that, in some of the graphs, there appears to be a steep increase or decrease in instability growth rate, then returning back to quasi-linear. These details will be discussed later.

The following plots contain 2 y-axes as well as a single x axis. The left y-axis is the voltage of the pressure sensor, and the right axis is the number of pixels. The two y-axes are graphed in relation to time on the x-axis. The time is measured in microseconds, voltage in millivolts, and pixels are the length of the pixels characterizing the instability amplitude for each frame. Due to the time delay and the frame rate discrepancy, there is a some uncertainty (on the order of the time interval between the frames) in the actual time that the shockwave hits the curtain.

Set 1:

The first set of graphs contain Mach number 1.2 with the 2mm curtain. This particular trial makes it possible to see the most frames, which ended up being over 20, and between 40. In this case, it seems as if the trend appears linear. The top view seems to match the same trend as the side view as well. Note that in this and subsequent images several features are noticeable in the pressure trace. In Figure 18, the shock arrives at the time mark about 10 ms, followed by the pressure wave. At about 15 ms, a rarefaction wave reflected off the wall of the driver section arrives, followed by the diffuse subsonic

pressure wave from the baffle box at about 23 ms. Similar features are present for other Mach numbers.

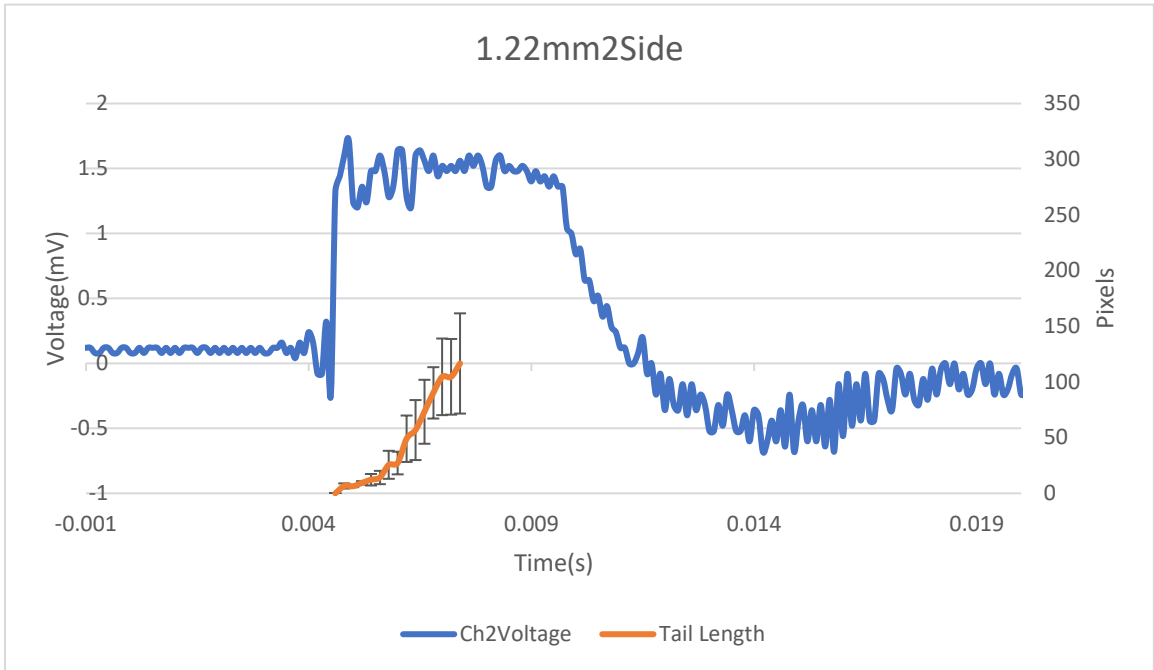


Figure 18: Side View Plot Mach 1.2 2mm Curtain

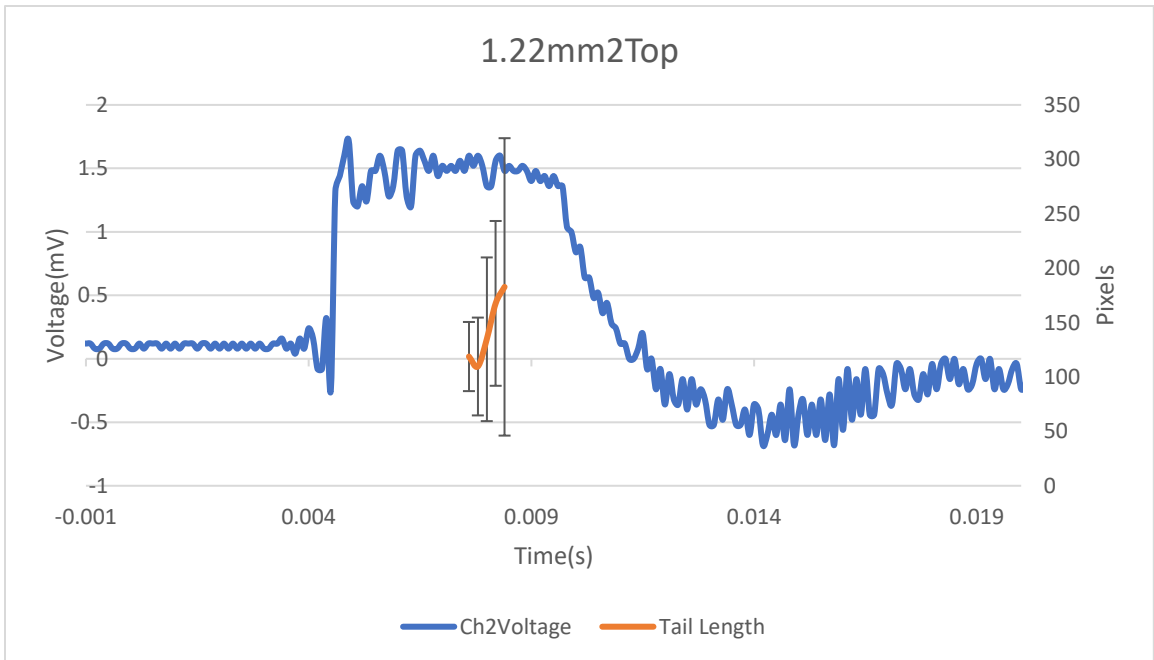


Figure 19: Top View Plot Mach 1.2 2mm Curtain

Set 2:

The second set of data contains the graphs for a 2mm curtain at 1.45 Mach. Unfortunately not as many data points can be gathered due to various reasons. Like the first set of trials the growth is found to be quasi-linear. The amount of frames gathered will stay between 6-12 for the duration of the graphs.

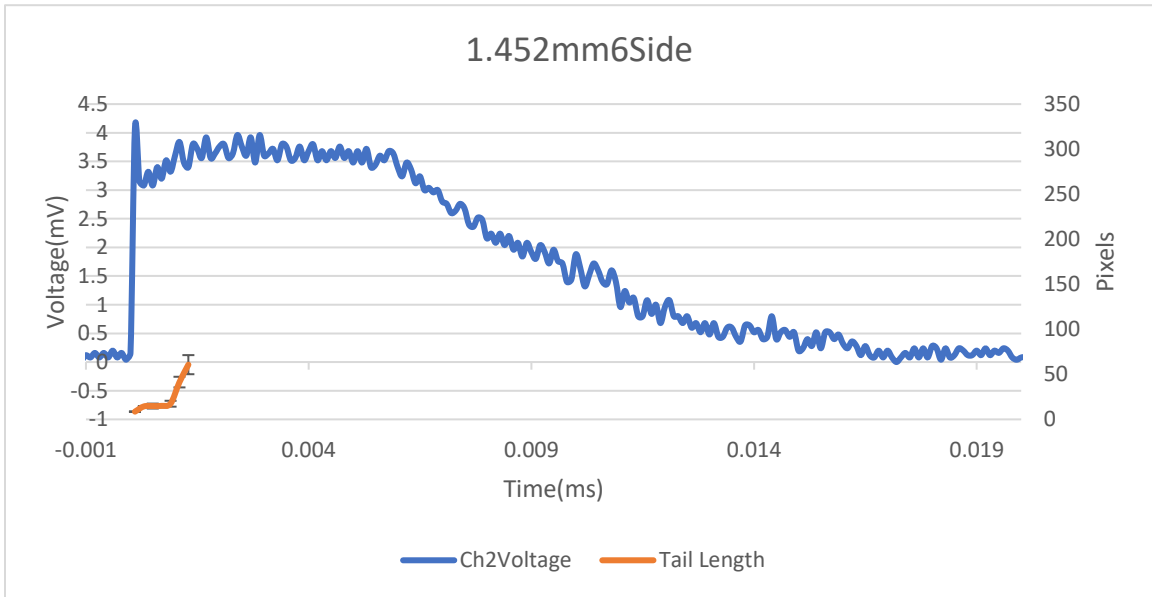


Figure 20: Side View Plot Mach 1.45 2mm Curtain

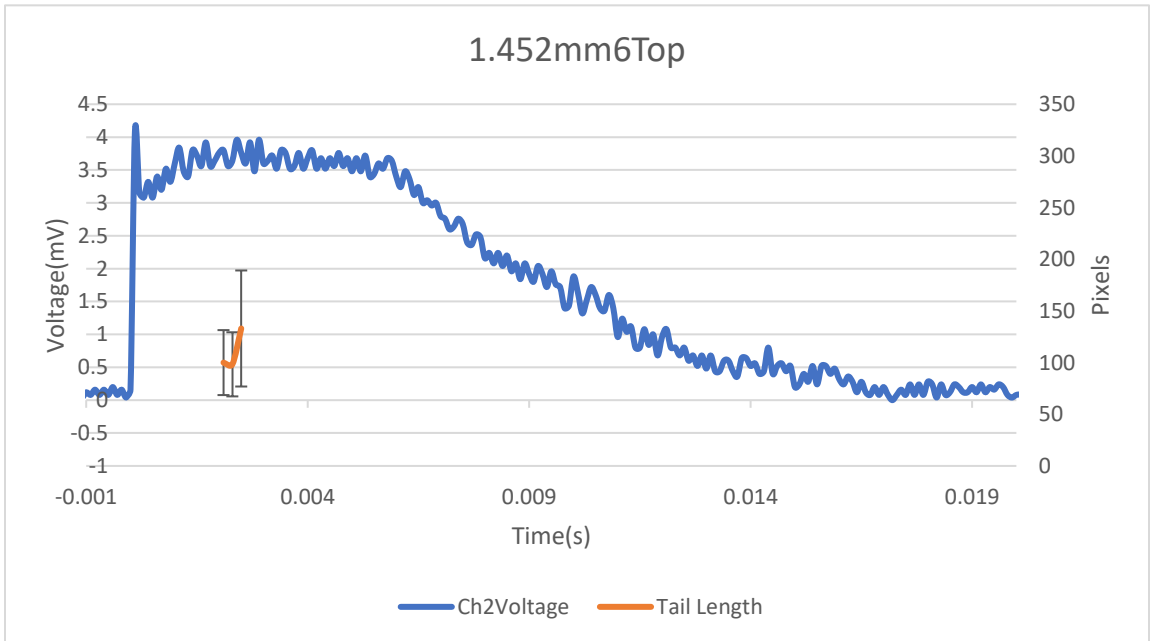


Figure 21: Top View Plot Mach 1.45 2mm Curtain

Set 3:

The third set consists of the 2 mm curtain data for the Mach number 1.7. The number of frames able to be captured is somewhere on the order of 3-10. Like the other two, the trend still seems to hold steady.

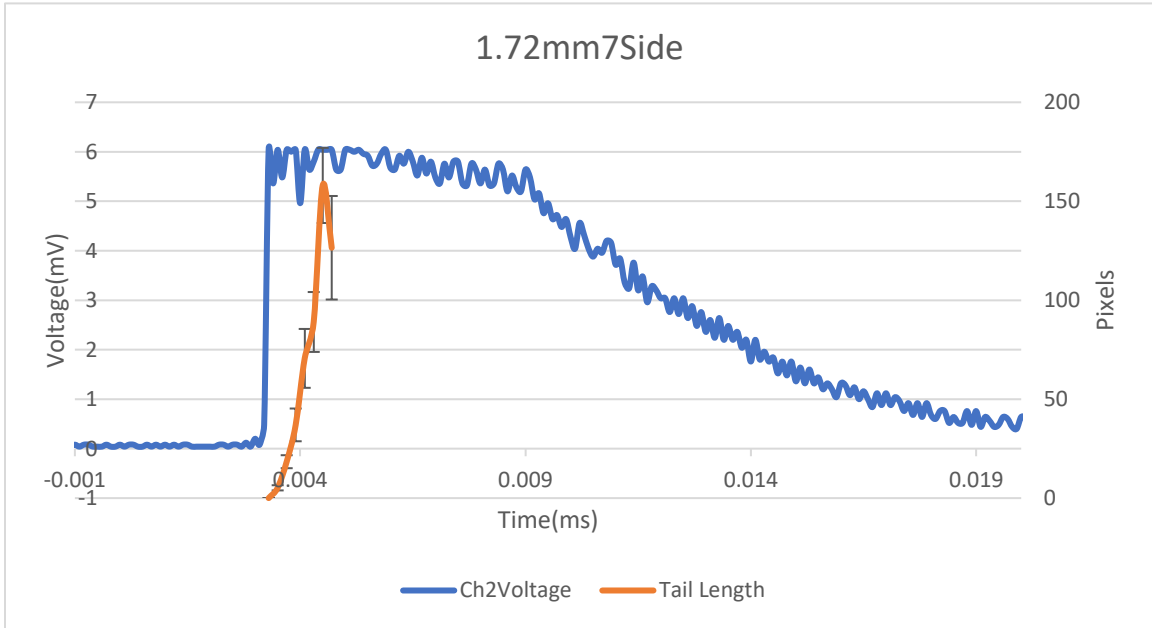


Figure 22: Side View Plot Mach 1.7 2mm Curtain

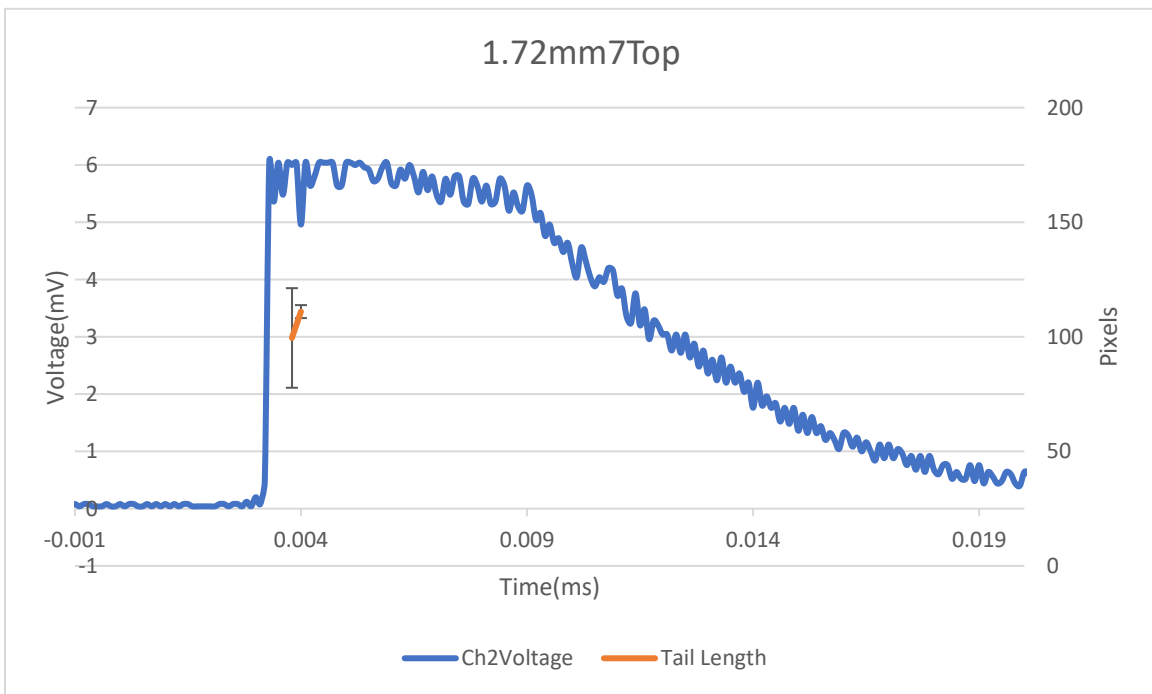


Figure 23: Top View Plot Mach 1.7 2mm Curtain

Set4:

The fourth set of data contains the pressure data and frames of the 6 mm curtain at a Mach number of 1.2. Again, the relative linearity is observed in the sequence. Most of the other graphs would show something similar, although not as clearly.

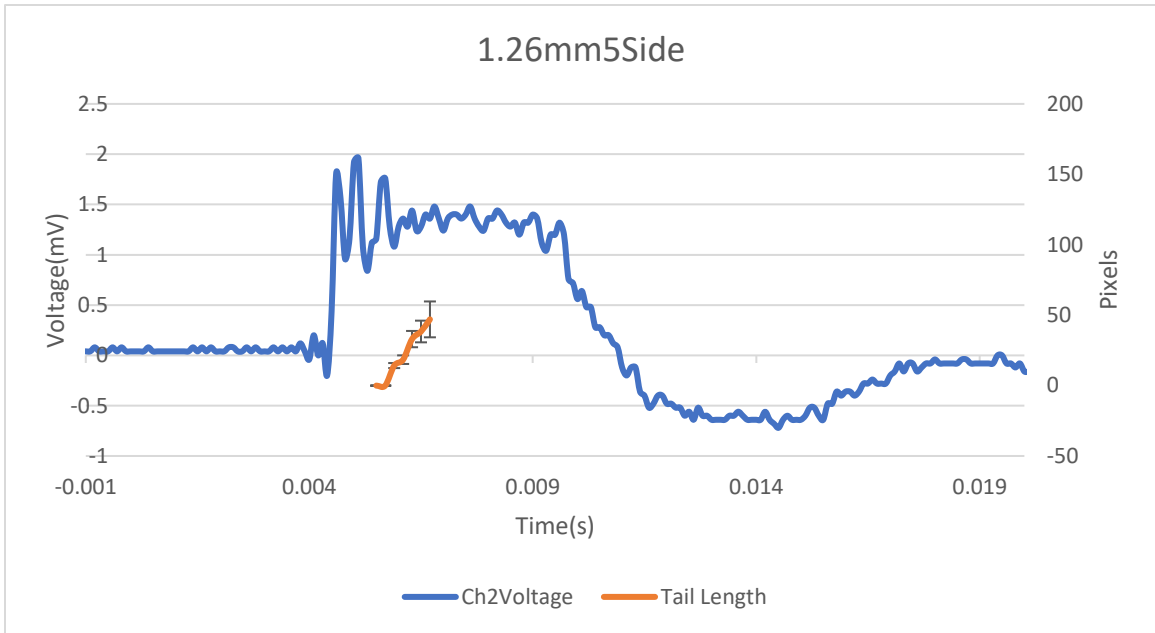


Figure 24: Side View Plot Mach 1.2 6mm Curtain

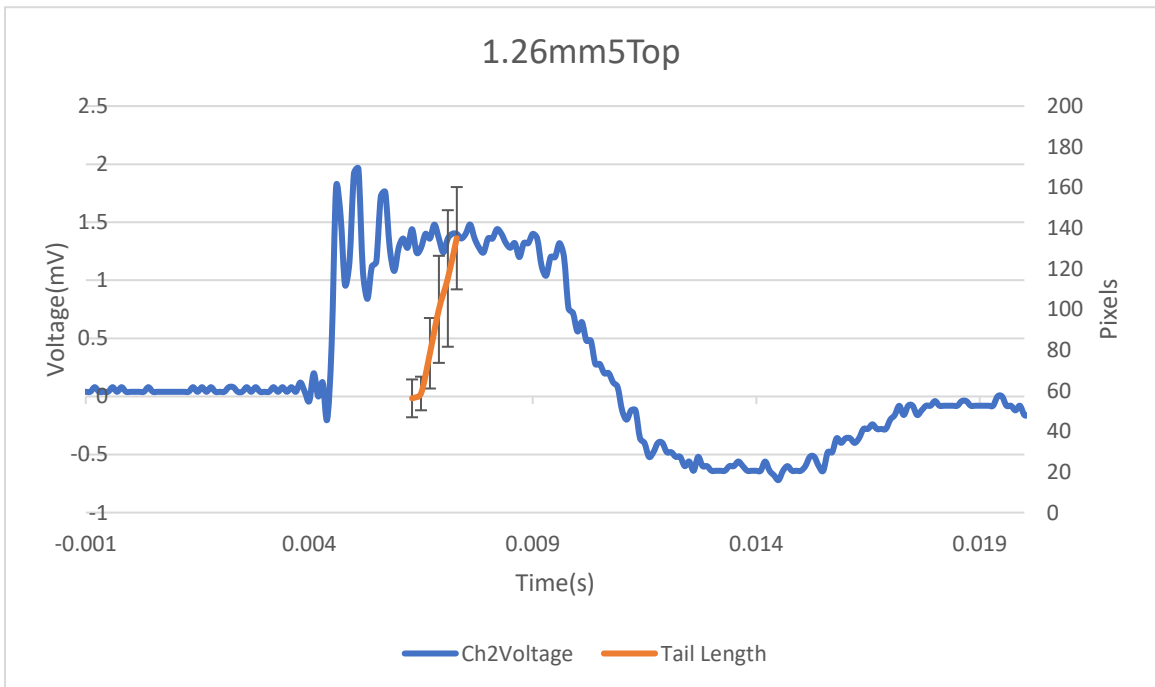


Figure 25: Top View Plot Mach 1.2 6mm Curtain

Set 5:

This set of characterizes the 6 mm curtain with Mach number of 1.45. The number of collected data points per graph is roughly 4-6. As seen in the other data sets the linearity can still be observed.

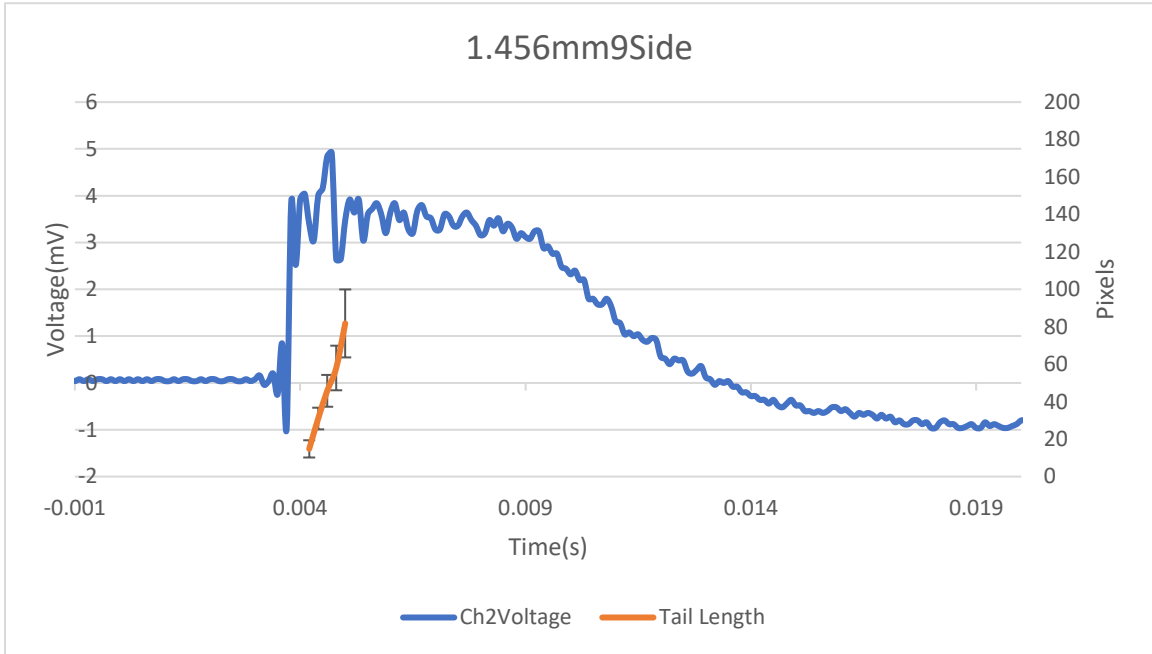


Figure 26: Side View Plot Mach 1.45 6mm Curtain

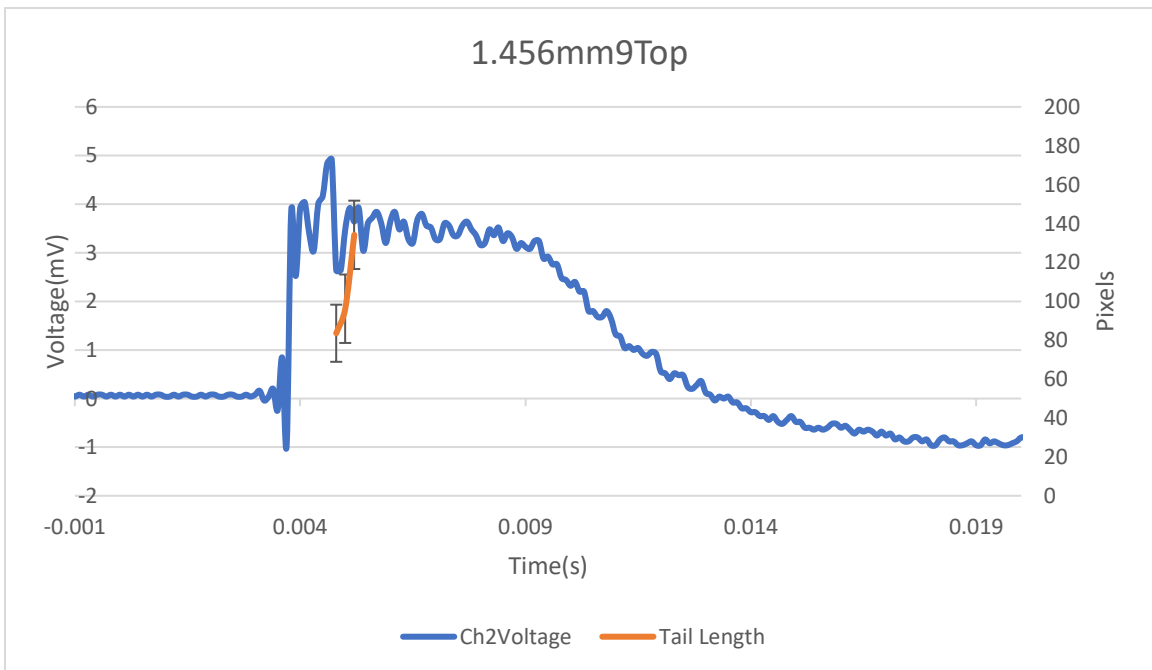


Figure 27: Top View Plot Mach 1.45 6mm Curtain

Set 6:

The last example of the data set contains the 6mm curtain at the Mach speed of 1.7. The last data set can still be observed producing a quasi-linear graph that is based on time.

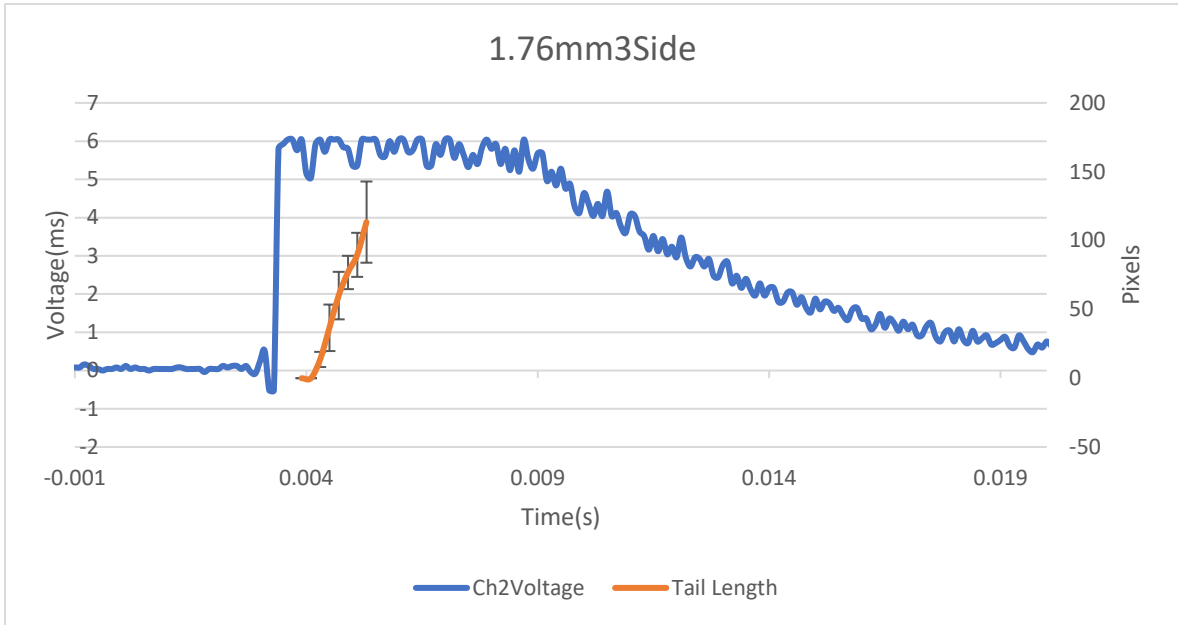


Figure 28: Side View Plot Mach 1.7 6mm Curtain

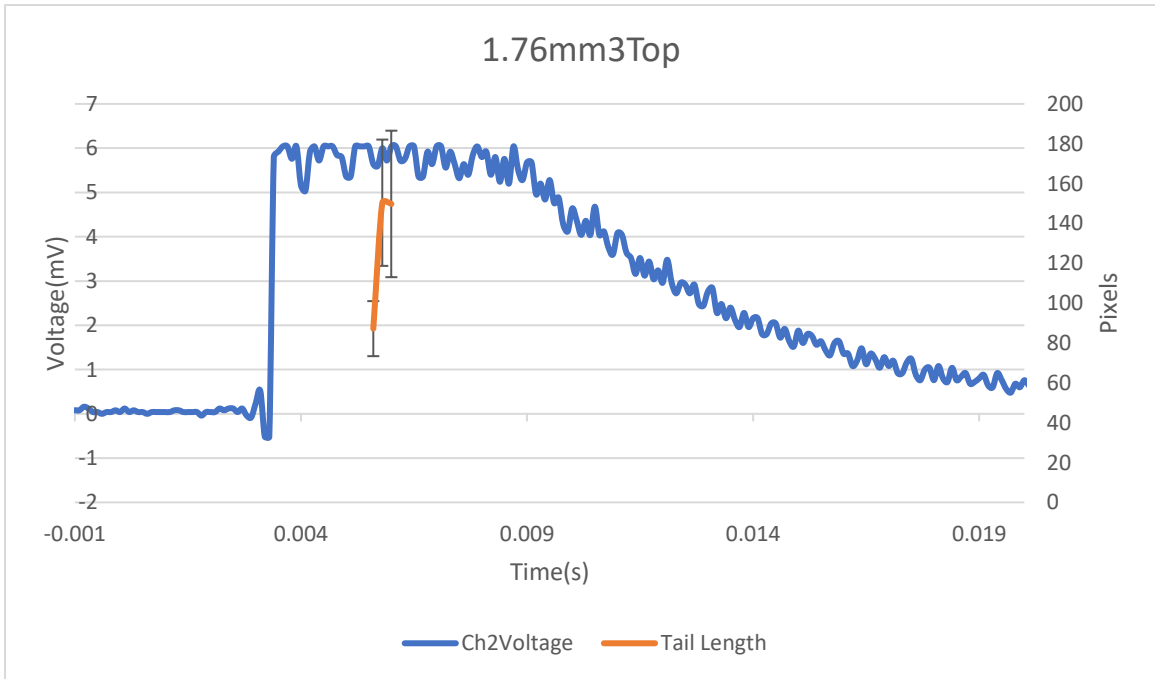


Figure 29: Top View Plot Mach 1.7 6mm Curtain

Chapter 5: Discussion

Section 5.1 Measuring Difficulties

As seen in the results above, there is a rough linearity characterizing the shock-driven instability amplitude growth, which can be seen between 40 and 10 frames in the video on the side of the tube. However, the measurement interval is limited by the camera field of view. This means the full frames are from between 12 and 8 frames after the shock is viewed. There is an exception in the first sequence of videos for Mach 1.2, 2 mm. This sequence was exceptionally clear, and up to 20 frames were seen.

Taking the measurements in the frames of the top view was somewhat difficult. It was found that, because it is a reflection and the widened view of the camera and the resolution is modest, there was a substantial amount of distortion in the viewing area. In addition, during the initial sequence with the 45-degree angle, it was not possible to see the early propagation of the instability in the top view because the bracket was in the way. From these batches of frames, a few data points could still be gathered from the top view.

Section 5.2 Differences and Non-linearity

The top view also appeared to show, in general, that the amplitude growth was slightly different. The likely reason for that is the scale difference of the curtain features in the vertical and horizontal directions: these features are stretched in the vertical direction as the curtain accelerates before shock arrival. The dominant wavelength of the instability is thus different in the two views. Due to the optical distortion in the top view,

not many top view data points could be gathered, but from what is seen, it seems to follow the same pattern of growth as the side view (see Figure 30).

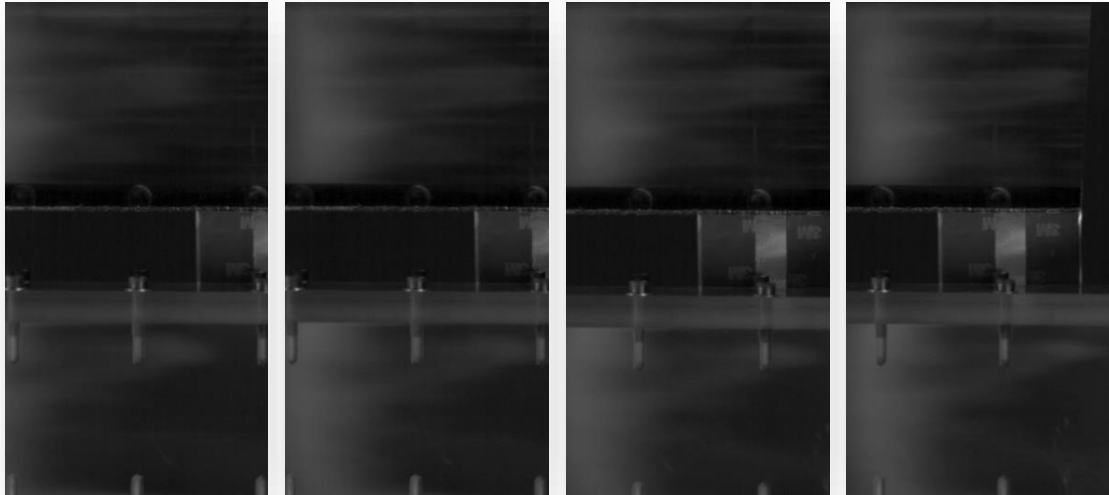


Figure 30: Frame Progression Combined View

Furthermore, something interesting occurred when data was being taken. At first, it was slightly unclear why some of the instability was not growing entirely linear. In a few frames, the instability growth rate either increased sporadically or dropped at eccentric intervals. Now, in observing the greater data set, this seemed to happen a number of times when the data was being graphed. This inconsistency seemed to be a bit uniform in where and how it occurred in the sequence of shocks. Interestingly, the time of the change in the instability growth rate appears consistent with the arrival of the rarefaction wave reflected off the driver section wall (Brouillette 2001). One of the features described in the review paper by Brouillette is that the rarefaction wave may actually change the growth of the instability entirely. It was intriguing to see this because there are some instances where this is not seen at all. It is unclear what the mechanism of

this would be and why it is only seen occasionally. Something else worth noting is that when particle regimes change, much of the physics changes, as discussed briefly about with the $A_m \sim 1$. Some of the videos show clusters lagging behind of what is assumed to be the heavier particles. This would also be indicative of the A_m numbers being close to 1 as the inertial effects begin to take precedence over the hydrodynamic ones. This would change the shape and behavior of the cloud instability propagation as discussed in (Probyn et al. 2021).

Additionally, it is worth noting is that, in several of the analyzed pressure traces, it was found that there was even some variation in the Mach numbers themselves. Some of the reasons may have been because of environmental inconsistencies like pressure and temperature in the lab. It can be recalled that, on several days, it was incredibly humid and hot. This may be affecting the pressure propagating throughout the tube. This may be another reason why there were inconsistencies showing some non-linearity for a frame and then returning to normal.

Finally, the most important observation is that for all the cases we observed there was an extensive (milliseconds) interval of the linear growth of the shock-driven multiphase instability. In comparison, the classical Richtmyer-Meshkov instability amplitude growth can be described by a quasi-logarithmic growth, and so is the shock-driven multiphase instability in the case of small particle size and small A_m (Vorobieff et al. 2011). The flow regime we investigate here ($A_m \sim 1$), in contrast, has a much higher role of particle inertia, which is the likely reason for the newly observed growth trend.

Section 5.3 Agreement with Numerical Modeling

In a paper written by (Han 2021) at the USC, numerically, it was found that at different times after a perceived shock interaction at the initial interaction, the particle curtain is hit by the shock it is a uniform sheet, prior to the interaction. As the shock contacts curtain, it creates a boundary where the particles own inertia acts on the pressure wave. This produces a density gradient of the particle curtain. Later in the propagation, because of the particle inertia, a leading and trailing edge begins to form. As the shock continues to propagate through the curtain, the particles begin to disperse through the shock tube. At the leading edge, the cloud is moving faster, and the trailing edge is slower. This leads to the width of the curtain becoming larger over time, with the growth being of a linear nature (Han 2021). What we can see is a quasi- linear relationship that roughly mimics the effect seen in the numerical model. Because of the previously stated environmental and mechanical factors, it did seem to deviate from this model with some rough agreement.

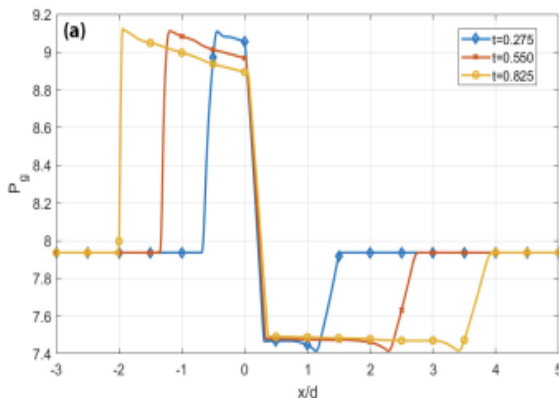


Figure 31: Pressure Projection(Han 2021)

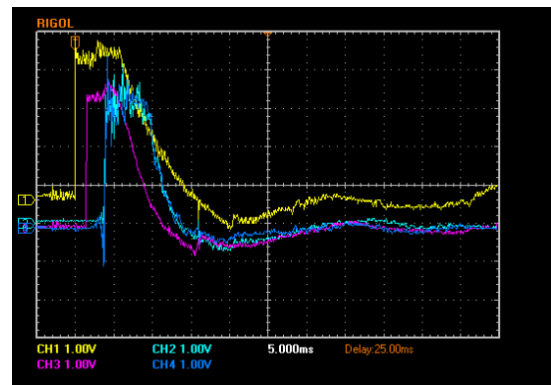


Figure 32: Pressure Trace Mach 1.45

In analyzing the pressure traces by inspection of the pressure graph from the experimental data, there is a close resemblance to the projected pressure graph from the paper above (see Figure 30 and 31). When the pressure trace is compared to the numerical calculation, it seems to show a resemblance to the 1.45 Mach test (Han 2021). In this regard, it seems to amp up from the transducer. Then, the pressure wave travels a bit, and then dips down below the 0 mark as there is a vacuum left in the wake that eventually recovers back to around zero. In addition, there are visual similarities between the graphical model from the paper as well. For example, in the videos taken, they seem to show some agreement of how the cloud expands and travels in the numerical model. After some duration, something close to the end of the propagation in the experiment, it looks very similar as shown (see Figures 32 and 33). This means that, at least qualitatively, the experimental data is consistent with the numerical data.

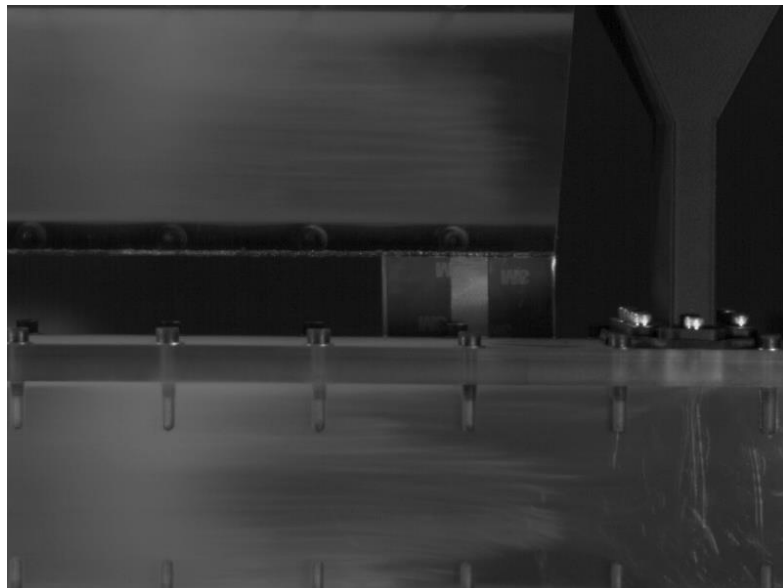


Figure 33: Cloud Expansion Length after Time

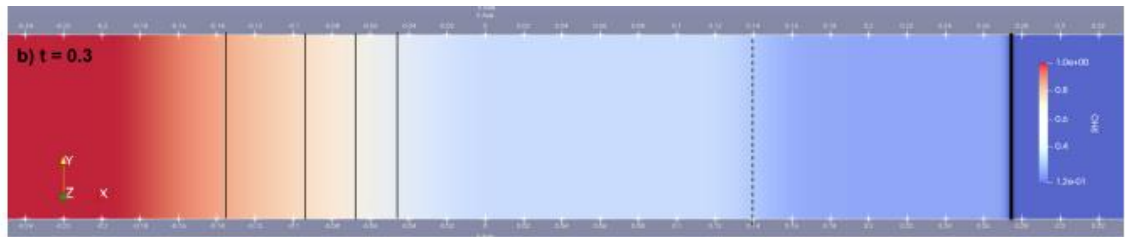


Figure 34: Theoretical Expanded Cloud(Han 2021)

Lastly, it is essential to note the effects of the shock. The striation growth is not meandering and rounded, or even mushrooming like in the RTI, M-RTI or RMI shock interactions, which is very interesting. This supports the earlier paper mentioned in that this is something different which has some of the markers of the RTI and RMI, the major difference is its quasi-linear growth (Ludwigsen et al. 2022; Vorobieff et al. 2020).

Chapter 6: Conclusion and Future work

Section 6.1 Conclusion

This thesis opened with a review of gravity- and shock-driven single- and multiphase instabilities. It has been shown that RMI, RTI, SDMI and M-RTI can all be a type of acceleration-driven instability, which occurs in fluid mixtures. For SDMI, it was noted that the regime of high multiphase Atwood numbers was relatively poorly understood.

Then a visualization system was described to facilitate the studies of SDMI with simultaneous two-plane visualization, and shock-tube experimental results presented for shock interaction with a falling particle curtain characterized by the multiphase Atwood number close to unity.

Results show that the quasi-linear SDMI instability growth manifests in both visualization planes and persists for milliseconds. These observations are consistent with the predictions of numerical modeling (Han 2021). Overall, the particles disperse in a spreading band-like pattern in the shock tube. After a certain number of frames, the cloud seems to move as a single aggregate of particles across the tube. Interestingly, and in addition, it is essential to note the fact that the heavier particles lag behind for some time even after the cloud is formed and it begins to move. This is indicative of a flow regime change as stated in (Vorobieff et al. 2020). However, there is only a certain degree of agreement, and more testing is necessary to see if this is really the case. Visual, pressure, and growth rate appear consistent.

Finally, if it could be definitively proven that the growth rate of the instability in shock driven particle-laden flows with high particle-mass loading is linear, it would mean that our notion of fluid mechanics as the driving physics of shocked flows could change to particle kinematics. Much of the shock driven multiphase systems deal with a momentum condition (Wang and Yan 2019). This could simplify the way numerical modeling is performed.

Section 6.2 Future Work

In many earlier experiments, only a single view is used (Orlicz, Balasubramanian, and Prestridge 2013). Adding the second view direction allows for a more accurate representation of particle and gas flow due to the shock wave in the test section. This allows for a two-dimensional calculation of groupings of particles or structure morphology like in the UNM 2010 experiment (Vorobieff et al. 2010). By using this method, we can now tell the behavior of particles and debris to better protect against or mitigate the effects of shock, or even predict gas mixing in combustion chambers as stated (Nair, Narayanan, and Suryan 2021a). Before, it was only possible to see the parameters of particles in a single directional plane. More importantly, because of the more accurate experimentation, this type of experiment has a high potential to validate many more simulation models in a 3-dimensional setting.

Further investigation needs to be carried out in this regard. These experiments seem to roughly point toward a linearity between the shock driven instability and the growth rate. The agreement only seemed to be rough and slightly inconsistent, which is why the term quasi is used. Assessment of the effect of the rarefaction wave is necessary

as this appears to change the particle movement. In addition, and as stated above, environmental factors would need to be controlled more tightly as this affects shock propagation through the tube.

As stated in the analysis section, the top and side views seemed to show differences in the growth trends. This difference needs to be studied further and related to any anisotropy in the initial conditions.

Additionally, for future work, it would be very beneficial to find out why the mirror in the third view was more stable when it was further from the shock wave. A possible new experiment might be to test what the distance may need to be to keep the mirror steady. A small piston motor or something along those lines with a PID controller might be something that could be used to provide a similar effect as the double-sided 3M tape.

References

- Anderson, M., P. Vorobieff, C. R. Truman, C. Corbin, G. Kuehner, P. Wayne, J. Conroy, R. White, and S. Kumar. 2015. "An Experimental and Numerical Study of Shock Interaction with a Gas Column Seeded with Droplets." *Shock Waves* 25 (2): 107–25. <https://doi.org/10.1007/s00193-015-0555-6>.
- Brouillette, Martin. 2001. "THE RICHTMYER-MESHKOV INSTABILITY." www.annualreviews.org.
- FFmpeg Developers. 2016. "Ffmpeg Tool."
- Freelong, Daniel M. 2021. "Interaction of a Shock Wave with a Particle Curtain."
- Han, Henry. 2021. "Discontinuous Galerkin-Based Particle-Source-in-Cell Solver for 1-D Compressible Particle-Laden Flows."
- I.G. Currie. 2013. *Fundamentals of Mechanics of Fluids, Fourth Edition*. CRC Press, Taylor and Francis Group.
- Ludwigsen, Josh, Patrick Wayne, Daniel Freelong, Gregory Vigil, Carolina Shaheen, Peter Vorobeiff, and C. Randall Truman. 2022. "Fractal Properties of a Falling Particle Curtain in Air." *Journal of Fluids Engineering, Transactions of the ASME* 144 (1). <https://doi.org/10.1115/1.4051543>.
- McFarland, Jacob A., Wolfgang J. Black, Jeevan Dahal, and Brandon E. Morgan. 2016. "Computational Study of the Shock Driven Instability of a Multiphase Particle-Gas System." *Physics of Fluids* 28 (2). <https://doi.org/10.1063/1.4941131>.
- Musci, Benjamin, Samuel Petter, Gokul Pathikonda, Bradley Ochs, and Devesh Ranjan. 2020. "Supernova Hydrodynamics: A Lab-Scale Study of the Blast-Driven Instability Using High-Speed Diagnostics." *The Astrophysical Journal* 896 (2): 92. <https://doi.org/10.3847/1538-4357/ab8f8f>.
- Nair, Prasanth P., Vinod Narayanan, and Abhilash Suryan. 2021a. "Combustion Efficiency Improvement for Scramjet Combustor with Strut Based Flame Stabilizer Using Passive Techniques." *International Journal of Hydrogen Energy* 46 (80): 40054–72. <https://doi.org/10.1016/j.ijhydene.2021.09.224>.
- . 2021b. "Combustion Efficiency Improvement for Scramjet Combustor with Strut Based Flame Stabilizer Using Passive Techniques." *International Journal of Hydrogen Energy* 46 (80): 40054–72. <https://doi.org/10.1016/j.ijhydene.2021.09.224>.
- Orlicz, G. C., S. Balasubramanian, and K. P. Prestridge. 2013. "Incident Shock Mach Number Effects on Richtmyer-Meshkov Mixing in a Heavy Gas Layer." *Physics of Fluids* 25 (11). <https://doi.org/10.1063/1.4827435>.

- Probyn, M. G., R. J.R. Williams, B. Thornber, D. Drikakis, and D. L. Youngs. 2021. "2D Single-Mode Richtmyer–Meshkov Instability." *Physica D: Nonlinear Phenomena* 418 (April). <https://doi.org/10.1016/j.physd.2020.132827>.
- Rahman, Mohammad, Daniel Freelong, Manuel Iglesias, Peter Vorobieff, and Rahman Team Sazedur. 2021. "Study of Shock Interaction with Non-Metallic Solid Bodies." *APS Division of Fluid Dynamics Meeting Abstracts Q03* (009).
- "RIGOL User's Guide DS1000B Series Digital Oscilloscopes." 2016. www.rigol.com.
- Schindelin, Johannes, Ignacio Arganda-Carreras, Erwin Frise, Verena Kaynig, Mark Longair, Tobias Pietzsch, Stephan Preibisch, et al. 2012. "Fiji: An Open-Source Platform for Biological-Image Analysis." *Nature Methods*. <https://doi.org/10.1038/nmeth.2019>.
- Shaheen, Carolina. 2023. "Diagnostics for Blast Interaction With Window Glass." Albuquerque: The University of New Mexico.
- "USER MANUAL CHRONOS 1.4 & CHRONOS 2.1-HD." n.d. <https://krontech.ca/chronos-2-1-resources>.
- Vorobieff, Peter, Michael Anderson, Joseph Conroy, Ross White, C. Randall Truman, and Sanjay Kumar. 2010. "Shock-Driven Hydrodynamic Instability Induced by Particle Seeding," November. <http://arxiv.org/abs/1011.1605>.
- . 2011. "Vortex Formation in a Shock-Accelerated Gas Induced by Particle Seeding." *Physical Review Letters* 106 (13). <https://doi.org/10.1103/PhysRevLett.106.184503>.
- Vorobieff, Peter, Paul M Rightley, and Robert F Benjamin. 1999. "Shock-Driven Gas Curtain: Fractal Dimension Evolution in Transition to Turbulence." *Physica D*. Vol. 133.
- Vorobieff, Peter, Patrick Wayne, Sumanth Reddy Lingampally, Gregory Vigil, Josh Ludwigsen, Daniel Freelong, C. Randall Truman, and Gustaaf Jacobs. 2020. "Formation of a Falling Particle Curtain." *International Journal of Computational Methods and Experimental Measurements* 8 (1): 27–35. <https://doi.org/10.2495/CMEM-V8-N1-27-35>.
- Wang, Zhao, and Hong Yan. 2019. "Unified Gas-Kinetic Scheme for the Monodisperse Gas-Particle Flow and Its Application in the Shock-Driven Multiphase Instability." *International Journal of Multiphase Flow* 119 (October): 95–107. <https://doi.org/10.1016/j.ijmultiphaseflow.2019.07.010>.
- Xu, Hai bin, Long kui Chen, De zhi Zhang, Fang ping Zhang, Zhao wu Shen, Wen xiang Liu, and Sheng hong Huang. 2021. "Mitigation Effects on the Reflected Overpressure of Blast Shock with Water Surrounding an Explosive in a Confined Space." *Defence Technology* 17 (3): 1071–80. <https://doi.org/10.1016/j.dt.2020.06.026>.
- Zhou, Ye, Robin J.R. Williams, Praveen Ramaprabhu, Michael Groom, Ben Thornber, Andrew Hillier, Wouter Mostert, et al. 2021. "Rayleigh–Taylor and Richtmyer–Meshkov Instabilities: A Journey through Scales." *Physica D: Nonlinear Phenomena*. Elsevier B.V. <https://doi.org/10.1016/j.physd.2020.132838>.

